Journal of Materials Chemistry A

ROYAL SOCIETY OF CHEMISTRY

PAPER

View Article Online
View Journal

Cite this: DOI: 10.1039/d0ta11137f

Functionalized metallic transition metal dichalcogenide (TaS_2) for nanocomposite membranes in direct methanol fuel cells†

Hossein Beydaghi,[a] Leyla Najafi,[b] Sebastiano Bellani,[b] Ahmad Bagheri,[a] Beatriz Martín-García,[a] Parisa Salarizadeh,[c] Khadijeh Hooshyari,[d] Sara Naderizadeh,[e] Michele Serri,[a] Lea Pasquale,[f] Bing Wu,[g] Reinier Oropesa-Nuñez,[h] Zdeněk Sofer,[g] Vittorio Pellegrini[ab] and Francesco Bonaccorso *[ab]

In this work, we designed a novel nanocomposite proton-exchange membrane (PEM) based on sulfonated poly(ether ether ketone) (SPEEK) and tantalum disulfide functionalized with terminal sulfonate groups (S-TaS_2). The PEMs are prepared through a solution-casting method and exploited in direct methanol fuel cells (DMFCs). Two-dimensional S-TaS_2 nanoflakes were prepared as a functional additive to produce the novel nanocomposite membrane for DMFCs due to their potential as a fuel barrier and an excellent proton conductor. To optimize the degree of sulfonation (DS) of SPEEK and the weight percentage (wt%) of S-TaS_2 nanoflakes in PEMs, we used the central composite design of the response surface method. The optimum PEM was obtained for SPEEK DS of 1.9% and a weight fraction (wt%) of S-TaS_2 nanoflakes of 70.2%. The optimized membrane shows a water uptake of 45.72%, a membrane swelling of 9.64%, a proton conductivity of 96.24 mS cm^{-1}, a methanol permeability of 2.66×10^{-7} cm^2 s^{-1}, and a selectivity of 36.18×10^4 S s cm^{-3}. Moreover, SPEEK/S-TaS_2 membranes show superior thermal and chemical stabilities compared to those of pristine SPEEK. The DMFC fabricated with the SPEEK/S-TaS_2 membrane has reached the maximum power densities of 64.55 mW cm^{-2} and 161.18 mW cm^{-2} at 30 °C and 80 °C, respectively, which are ~78% higher than the values obtained with the pristine SPEEK membrane. Our results demonstrate that SPEEK/S-TaS_2 membranes have a great potential for DMFC applications.

Received 15th November 2020
Accepted 8th January 2021

DOI: 10.1039/d0ta11137f

rsc.li/materials-a

1. Introduction

Among different types of energy conversion devices, direct methanol fuel cells (DMFCs) represent powerful clean energy devices due to their high energy conversion efficiency (>80%), simple structural design, extensive applications, and environmentally friendly operation.[1,2] Compared to proton-exchange membrane fuel cells, DMFCs can offer more flexible cell designs, together with high-safety and low cell cost. Moreover, methanol is currently a fuel that is more viable than hydrogen in terms of storage safety for portable devices.[3] In order to maximize both the final performance and durability of DMFCs, it is pivotal to minimize the fuel (methanol) transfer through the proton-exchange membrane (PEM).[4] Therefore, the PEM is a major key component in determining the ultimate performance of DMFCs.[5] Ideally, PEMs used in DMFCs must meet concomitant requirements, including high water uptake (WU), low membrane swelling (MS ≤ 10%), low methanol permeability ($P \leq 10^{-7}$ cm^2 s^{-1}), high proton conductivity ($\sigma \geq 80$ mS cm^{-1} at room temperature), and both electrochemical and mechanical stabilities during cell operation.[6–8] Currently, the most commonly used PEMs are perfluorinated (Nafion) membranes because they exhibit optimal thermal and chemical stabilities and high σ (~90 mS cm^{-1} at room temperature).[9,10] However, the ever-growing market competition between fuel–electrical energy conversion systems is driving the DMFC technology toward the search of PEMs alternative to Nafion, aiming to decrease both the material cost (~180 US$ per m for Nafion 117 and an annual production of 100 000 m^2)[11] and methanol crossover while providing superior mechanical stability and σ, especially at high temperatures (≥80 °C) at which water evaporation occurs.[12,13]

[a]Graphene Labs, Istituto Italiano di Tecnologia, via Morego 30, 16163 Genova, Italy
[b]BeDimensional SpA, via Albisola 121, 16163 Genova, Italy. E-mail: f.bonaccorso@bedimensional.it
[c]High-Temperature Fuel Cell Research Department, Vali-e-Asr University of Rafsanjan, 7718897111 Rafsanjan, Iran
[d]Department of Applied Chemistry, Faculty of Chemistry, Urmia University, 5756151818 Urmia, Iran
[e]Smart Materials, Istituto Italiano di Tecnologia, via Morego 30, 16163 Genova, Italy
[f]Materials Characterization Facility, Istituto Italiano di Tecnologia, via Morego 30, 16163 Genova, Italy
[g]Department of Inorganic Chemistry, University of Chemistry and Technology Prague, Technická 5, 166 28 Prague 6, Czech Republic
[h]Department of Materials Science and Engineering, Uppsala University, Box 534, 751 03 Uppsala, Sweden

† Electronic supplementary information (ESI) available. See DOI: 10.1039/d0ta11137f

In this context, different polymers have been investigated for the development of novel types of PEMs.[14,15] Unfortunately, none of them has fulfilled all the membrane requirements needed for their widespread commercialization.[16] To overcome the intrinsic limits of pristine polymers, nanocomposite membranes have attracted great interest for the preparation of advanced PEMs for DMFCs.[17–19] In particular, the use of poly(ether ether ketone) (PEEK) has increased dramatically in recent years, due to its ease of preparation, optimal thermal and chemical stabilities and excellent methanol barrier ($\sim 10^{-8}$ cm^2 s^{-1}).[20–22] Nevertheless, the lack of proton-conducting groups in the PEEK structure severely limits the final performance of DMFCs.[23] To overcome this problem, sulfonation of PEEK has been proposed as an effective approach.[24] Unlike Nafion, in sulfonated PEEK (SPEEK), the –SO_3H groups are attached directly to the aromatic backbone.[25] Consequently, the separation between hydrophilic/hydrophobic domains is reduced compared to the one in Nafion.[25] Meanwhile, SPEEK retains a low P ($\sim 10^{-7}$ cm^2 s^{-1}) due to its specific structure (hydrophobic backbone with hydrophilic branches and less hydrophobic/hydrophilic domains), representing a great advantage compared to other proposed Nafion alternatives.[26] Noteworthily, many properties of the sulfonated polymer have a direct relation to the degree of sulfonation (DS), which is defined as the number of sulfonic acid groups on the polymer structure.[27] The DS value of the polymer can be controlled by the concentration of acid (typically sulfuric acid, H_2SO_4), reaction time, and temperature used to perform the polymer sulfonation.[27] Importantly, the WU and σ of the membrane increase with increasing DS.[28] However, excessive DS (typically $\geq$75%) results in a decrease of both dimensional and mechanical stabilities of the membranes, as well as an increase of P, drastically deteriorating the DMFC performance.[28] Therefore, it is important to optimize the DS in order to obtain the most convenient property trade-off for the DMFCs. To overcome the dichotomy of membrane properties, the addition of fillers to SPEEK with mechanical strength and barrier properties may allow high-DS SPEEK to be developed while retaining optimal MS and P of the membrane.

Two-dimensional (2D) materials represent a class of potential fillers for the polymer used in PEMs.[29,30] Recently, different 2D materials in the form of nanosheets, including graphene oxide,[31] sulfonated graphene oxide,[32] sulfonated graphene oxide/iron oxide,[33] and sulfonated graphene oxide/iron titanate,[34] have been successfully used to produce nanocomposite membranes effective for DMFCs. Among 2D materials, transition metal dichalcogenides (TMDs), such as group-6 elements (*i.e.*, MX_2, in which M = Mo or W and X = S, Se or Te), represent an intriguing class of fillers, which can be functionalized by covalent attachment of functional groups at defect sites (*e.g.*, the edge site in the 2H phase of MoS_2) facilitating the electron transfer.[35,36] In addition, the functionalization of group-6 TMDs could also rely on the electron transfer between the electron-rich metallic phases (*e.g.*, 1T in MoS_2) and reactant precursors.[37] Based on this last consideration, we rationalized that group-5 TMDs, based on M = Ta, Nb or V, can be efficiently functionalized with sulfonated groups, thanks to the metallic character of their natural stable phases. For the particular case of 2D TaS_2, several metallic polytypes (*e.g.*, 2H-TaS_2,[38,39] 3R-TaS_2 [40] and 6R-TaS_2 [41]) have been successfully synthesized and used in energy conversion applications, thanks to their high surface area, catalytic activity of the basal planes and (electro) chemical stability in aqueous (acidic) media. Similarly to other 2D materials,[42,43] the morphology of TaS_2 nanoflakes is expected to act as a barrier against the fuel diffusion into the hosting polymer matrix. This results in a decrease of P of the nanocomposite membrane even in the presence of high-DS polymers, which intrinsically guarantee high σ.[32] In addition, the incorporation of sulfonated groups by the functionalization of metallic TaS_2 nanoflakes, leading to TaS_2 functionalized with sulfonated groups (S-TaS_2), can also impact positively on their proton-conducting ability, further enhancing the σ of the hosting polymer.[44] Besides, the presence of sulfonated groups in the TaS_2 nanoflakes improves the dispersion of nanoflakes in the most polar solvent used to process the polymer applied in DMFC membranes,[18] thus allowing the fillers to be homogeneously dispersed in the hosting polymeric matrix. Meanwhile, the interfacial interactions and the formation of hydrogen bonding between sulfonated groups of nanoflakes and functionalized groups of SPEEK should promote the compactness of the PEM structure, increasing the dimensional and thermal stabilities of nanocomposite membranes.[45]

In this work, we report the production of novel S-TaS_2 nanoflakes, obtained from the liquid-phase exfoliation (LPE) of 6R-TaS_2 crystals,[41] followed by functionalization with a mercaptopropane sulfonate, to fabricate a nanocomposite PEM by the solution-casting method for DMFC applications. The optimal amount of S-TaS_2 nanoflakes and DS of SPEEK are determined by means of response surface methodology (RSM), representing an effective group of statistical methods solving multivariate equations to predict the effect of multiple independent (*e.g.*, DS and wt% of S-TaS_2) and dependent variables (*e.g.*, WU, MS, P, S and σ) on the membrane performance.[46,47] Therefore, this method avoids jeopardizing experiments with excessive number of tests based on the multiple combination of parameters.[46,47] Using Central Composite Design (CCD)[48] in design of experiment (DOE) software[49] as the experimental design for our multivariable system (see ESI, S1.5†), the membranes were optimized to maximize WU, σ and selectivity (S) while minimizing MS and P, aiming to reach the optimum power density. The synthesis procedure together with structural, physical, chemical, and electrochemical properties of the as-produced nanocomposite membranes is discussed and compared with the results obtained with Nafion and other SPEEK-based membranes. Finally, our nanocomposite membranes are validated in DMFCs, demonstrating the effectiveness of S-TaS_2 fillers to simultaneously achieve low P, high σ and S and overcome the performance of DMFCs based on pristine SPEEK.

2. Results and discussion

2.1. Characterization of TaS_2 and S-TaS_2 nanoflakes

The 6R-TaS_2 crystals were synthesized by the direct reaction of atomic elements (see Experimental section in the ESI† for details), following a protocol previously reported by our group.[41] Noteworthily, the 6R polytype alternates layers with trigonal prismatic and octahedral Ta coordination[50] [similarly to 4H*b*-

TaS_2 [51]. Therefore, this mixed coordinated polytype can show properties resembling those exhibited by both trigonal prismatic (2H or 3R) and octahedral (1T) phases.[52]

The scheme of the functionalization procedure of TaS_2 nanoflakes, as supported hereafter by extensive material characterization (in particular, X-ray photoelectron spectroscopy (XPS) analysis), is shown in Scheme 1. The morphology of S-TaS_2 nanoflakes was investigated by transmission electron microscopy (TEM) analysis. As shown in Fig. 1a, the S-TaS_2 nanoflakes show irregularly shaped wrinkled structures, with the lateral size distributed between 10 and 400 nm, mainly <100 nm (Fig. 1b). The morphology of S-TaS_2 nanoflakes is therefore similar to the ones previously determined for the LPE-produced TaS_2 nanoflakes.[41] The phase of TaS_2 and S-TaS_2 nanoflakes was evaluated by X-ray diffraction (XRD) measurements. The XRD patterns of bulk TaS_2, TaS_2 nanoflakes and S-TaS_2 nanoflakes show diffraction peaks at around 14.2°, 29.6°, 45.9° and 62.6°, which correspond to the planes of hexagonal 6R phase (ICSD-52117).[41] The (002) peak (full width at half maximum (FWHM) = 1.06°) in TaS_2 nanoflakes is broader than that at 6R-TaS_2 crystals (FWHM = 0.18°) because of the smaller crystalline domains of TaS_2 nanoflakes. As 6R- and 2H-TaS_2 show similar X-ray diffraction (XRD) patterns (see reference cards, *i.e.*, ICSD-68488 for 2H-TaS_2 and ICSD-52117 for 6R-TaS_2),[41] one of the TaS_2 nanoflakes could also include a contribution from the 2H phase, which can also form during the 6R-TaS_2 exfoliation process.[41] The intensity of other peaks, despite maintaining the position, is strongly reduced, indicating that the TaS_2 nanoflakes preserve their crystal structure.[53] As shown in Fig. 1c, the S-TaS_2 nanoflakes exhibit a diffraction pattern similar to that of TaS_2 nanoflakes. Thus, the functionalization of TaS_2 nanoflakes does not change their phase. Raman analysis was carried out to investigate the structural properties of exfoliated nanoflakes (Fig. 1d). The as-synthetized 6R-TaS_2 crystals display a Raman spectrum that combines the mode of both the well-studied 2H- and 1T-phases. In fact, the layers with trigonal prismatic Ta coordination can show the out-of-plane vibration mode A_{1g} at ~380 cm^{-1}, the in-plane vibrational mode $E_{2g}{}^1$ at ~280 cm^{-1}, and the broad second-order peak attributed to the two-phonon process at ~180 cm^{-1}.[41,54,55] The layers with octahedral Ta coordination can display fold-back optical modes at ~250, ~310 and ~380 cm^{-1} arising from the formation of commensurate domains at room temperature.[56–59] After exfoliation, the samples still show the same Raman modes; the modes at 310 cm^{-1} is blue-shifted, likely because of the decrease of the long-range Coulombic interlayer interactions with decreasing number of layers.[38,60] Since the Raman modes of native crystals are present in exfoliated materials, these results indicate that the LPE and functionalization processes do not significantly alter the crystal structure of the starting material.

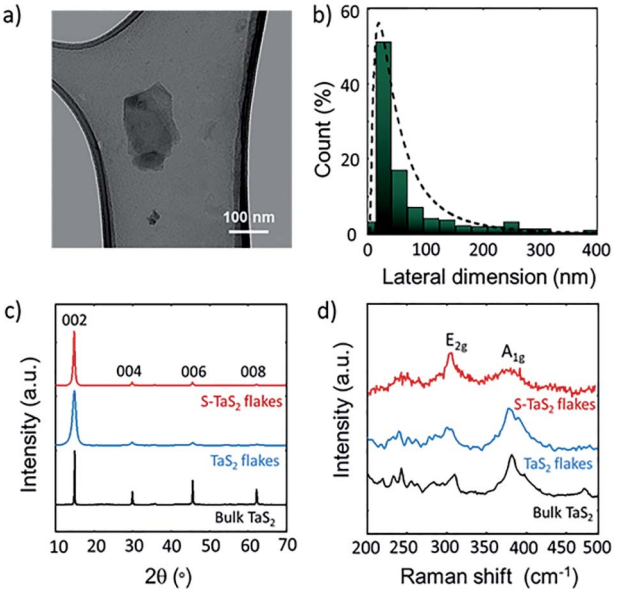

Fig. 1 (a) TEM image of S-TaS_2 nanoflakes. (b) TEM statistical analysis of the lateral dimension of S-TaS_2 nanoflakes. (c) XRD patterns and (d) Raman spectra (excitation wavelength = 532 nm) of bulk TaS_2 (in black), exfoliated TaS_2 nanoflakes (in blue), and S-TaS_2 nanoflakes (in red).

The elemental analysis and composition of exfoliated materials were evaluated through XPS measurements. Fig. 2a and c reports the XPS Ta 4f spectra of TaS_2 and S-TaS_2 nanoflakes, respectively, while the measured S 2p spectra are reported in Fig. 2b and d. The ratio between S and Ta estimated for TaS_2 nanoflakes is 0.64, as estimated from the XPS data (Fig. 2a and b). The observed S depletion is ascribed to the Ta oxidation. In agreement with previous experimental studies on

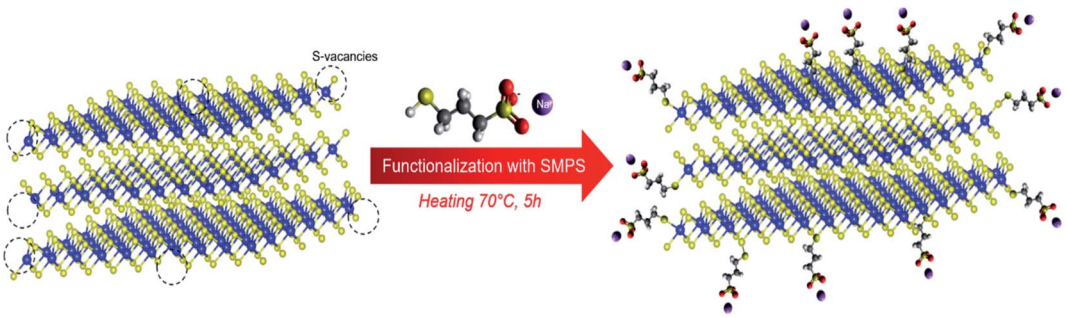

Scheme 1 Representative sketch of functionalization of TaS_2 nanoflakes by linking the thiol group of sodium 3-mercapto-1-propane sulfonate salt (SMPS) molecules to TaS_2 *via* S–S bonding or S-vacancy passivation.

group-5 TMDs,[38,41,61–63] the oxidation of Ta is mainly localized to the surface of nanoflakes. For this reason, Raman spectroscopy and XRD measurements, being less surface sensitive than the XPS, have not revealed any oxide-related features. The Ta 4f region of the XPS spectrum of TaS_2 nanoflakes (Fig. 2a) shows an intense doublet that peaked at 26.1 and 28.0 eV corresponding to Ta(+5) surface oxides.[64] The multidoublet component, with main peaks at 22.7 and 23.4 eV, corresponds to Ta(+4) in TaS_2 nanoflakes.[41,65] Previous studies revealed that the XPS Ta 4f spectrum of 6R-TaS_2 crystals resembles the one of 1T-TaS_2, in which two doublets assigned to Ta(+4) originated from periodic atomic displacements of room temperature nearly commensurate with charge density wave phase.[66,67] However, after exfoliation, the 2H phase can also emerge, leading to a dominant peak at the lowest binding energy at ~22.7 eV.[68,69] A small peak corresponding to O 2s, with an area constrained to ~5% of the O 1s one, was found by the fitting process at 23.5 eV. Noteworthily, sub-oxide can also contribute with doublets located between the Ta(+4) and Ta(+5) ones, broadening the fitted components.[70]

The S 2p region of the XPS spectrum of TaS_2 nanoflakes (Fig. 2b) exhibits multiple doublet components that were attributed to S(−2) in octahedral TaS_2 coordination (160.8 and 162.0 eV),[69,71] S(−2) in trigonal prismatic TaS_2 coordination (161.3 and 162.5 eV),[68,69] S(−2) near S vacancies (161.9 and 163.1 eV),[72–74] S in homopolar S–S bonds (163.3 and 164.5 eV),[75] and finally highly oxidized sulfur states S(+4) (166.4 and 167.6 eV) and S(+6) states (168.4 and 169.6 eV).[76–78] Fig. 2c and d shows the Ta 4f and S 2p spectra, respectively, measured for S-TaS_2 nanoflakes. The Ta 4f region exhibits the TaS_2-related doublets with main peaks at 22.8 and 23.7 eV, as well as a pair of doublets corresponding to Ta oxide (26.4 and 28.3 eV) and sub-oxide (Ta_2O_{5-x}) (25.4 and 27.3 eV),[64] plus a minor O 2s component (23.5 eV). Compared to the TaS_2 nanoflakes, the oxidized component (oxide and sub-oxide) of S-TaS_2 nanoflakes is significantly reduced by ~28% relative to the total Ta 4f signal. This could be the result of the passivation of S vacancies preventing Ta reaction with oxygen. In the S 2p spectrum, the S(−2) peaks are broadened compared to those of TaS_2 (with FWHM of 1.1 and 0.6 eV of S-TaS_2 and TaS_2 nanoflakes, respectively). Consequently, the components attributed to octahedral and trigonal prismatic coordination in alternating layers of the 6R structure are not distinguishable. In addition, the intensity of the oxidized S states, *i.e.*, S(+4) and S(+6), is drastically reduced compared to the case of pristine TaS_2 nanoflakes. The S–Ta ratio estimated for the S-TaS_2 nanoflakes is 0.97. This result indicates an S enrichment in comparison to the TaS_2 nanoflakes, which means that the functionalization step and the subsequent washing/centrifugation process have purified the starting material. By attributing the amount of S(+4) to the sulfonate group of the SMPS molecule, the degree of SMPS functionalization in S-TaS_2 nanoflakes (*i.e.*, SMPS molecules per Ta atom) has been estimated at ~3%.

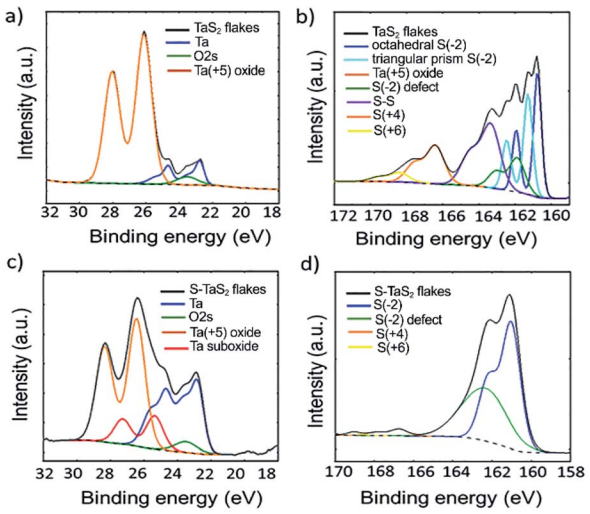

Fig. 2 XPS spectra of (a) Ta 4f signals of exfoliated TaS_2 nanoflakes. (b) S 2p signals of exfoliated TaS_2 nanoflakes. (c) Ta 4f signals of S-TaS_2 nanoflakes and (d) S 2p signals of S-TaS_2 nanoflakes.

2.2. Characterization of the S-TaS_2-based nanocomposite membrane

The procedure (solution-casting method) used to fabricate the TaS_2- and S-TaS_2-based nanocomposite membranes is detailed in ESI (Section S1.4).† Noteworthily, the incorporation of pristine TaS_2 nanoflakes in the SPEEK matrix resulted in highly inhomogeneous membranes with particle aggregates visible to the eye. In fact, the lack of functional group on the surface of pristine TaS_2 nanoflakes impedes the dispersion of TaS_2 nanoflakes in the polar solvent used to process the SPEEK. Moreover, the absence of a functional sulfonated group in TaS_2 nanoflakes weakens the interfacial interactions, such as the hydrogen bonding between the nanoflakes and SPEEK, leading to a dimensional instability of the nanocomposite membrane. Therefore, it was not possible to test SPEEK/TaS_2 nanocomposite membranes in DMFCs. Contrarily, the S-TaS_2 nanoflakes can be homogeneously dispersed in the SPEEK matrix, thanks to the strong interfacial hydrogen bonding between the sulfonated groups of S-TaS_2 nanoflakes and polymer chemical groups. Therefore, only SPEEK/S-TaS_2 membranes were characterized and subsequently tested in DMFCs, as reported in the following sections.

2.2.1 Membrane water uptake and swelling. According to the key role of water molecules in σ, P, and final performance of the produced membranes, the WU and MS of the investigated membranes, *i.e.*, the SPEEK/S-TaS_2 membranes (M_{runx}), were measured for their optimization (see details in the Experimental section in the ESI†). Typically, high values of WU translate into high σ due to the proton sorption by free water molecules available on the structure of the membrane.[79] However, the polymer commonly used for PEMs have different optimum amounts of WU to maximize the ion transfer. In particular, excessive WU can lead to the closure of the ion transfer channels in the structure of the polymer and poor performance due to membrane softening and water flooding.[80] In addition, high WU can cause an excessive MS of the membrane, which reduces its dimensional stability.[81] Thus,

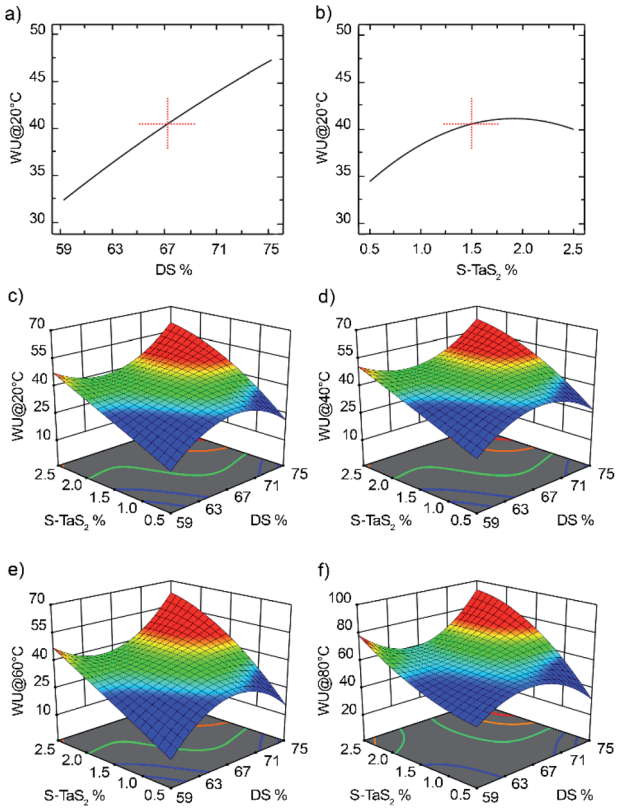

Fig. 3 One-factor effect plots illustrating the influence of: (a) DS of SPEEK on WU@20 °C at 1.5 wt% of S-TaS_2 nanoflakes; (b) wt% of S-TaS_2 nanoflakes on WU@20 °C at the DS of SPEEK of 67.50%. 3D-surface plots of WU *versus* DS of SPEEK and wt% of S-TaS_2 nanoflakes in the nanocomposite membranes, at the temperatures of (c) 20, (d) 40, (e) 60, and (f) 80 °C.

control of the WU is critical to achieve optimal σ, and even ideal P.

Fig. 3 and Table 1 show the WU measured for M_{runx} at different temperatures, *i.e.*, 20, 40, 60, and 80 °C. In more detail, Fig. 3a and b shows the dependence of WU (measured at 20 °C) on the DS of SPEEK (at 1.5 wt% of S-TaS_2 nanoflakes) and wt% of S-TaS_2 nanoflakes (at the DS of SPEEK of 67.50%), respectively. As shown in Fig. 3f, the trend of WU with increasing DS of polymer and wt% of nanoflakes is similar at different temperatures (Fig. 3c–f). Overall, the WU increases with the increase of DS content of SPEEK from 60 to 75 wt%, reaching a maximum value of 47.35 for M_{run8}. The dependence of WU on the DS of polymer is attributed to the enhancement of hydrophilicity of polymer in the presence of the SO_3H group introduced by the sulfonation process.[82] Moreover, the WU also increases with increasing amount of S-TaS_2 nanoflakes from 0.5 to 2 wt%. This means that the hydrophilic nature of S-TaS_2 nanoflakes, likely attributed to the formation of hydrogen bonding between sulfonated groups of nanoflakes and free water molecules, improves the water retention properties of pristine SPEEK.[83] However, the addition of more than 2 wt% of S-TaS_2 nanoflakes slightly reduces the WU of the membranes, probably due to the closure of transport channels of the membrane caused by increasing the compaction of the membrane structure as well as S-TaS_2 nanoflake aggregation. For all the prepared membranes, the WU value increased with temperature due to the increase of mobility of free water molecules and polymer chains that facilitates water absorption in the polymeric backbone.[84] The MS is a key parameter affecting the lifetime of the PEMs. It is desirable that the membranes possess a high WU while retaining dimensional stability (*i.e.*, low MS).[85] The MS values measured for M_{runx} are shown in Fig. 4 and Table 1. The MS of the membranes increases with the increase of DS of SPEEK, reaching a minimum value of 5.18 for M_{run10}, as expected by the WU trend (the higher the WU, the higher the MS). In addition, the MS of the membranes decreases with the increase of wt% of S-TaS_2 nanoflakes. The highest wt% of S-TaS_2 nanoflakes shows the lowest MS at constant DS of polymer due to the reduction of free volume in the structure of the membrane with formation of hydrogen bonding between functionalized groups of nanoflakes and sulfonated groups of SPPEK.[31,86] In fact, the formation of strong hydrogen bonding between sulfonated groups of nanoflakes and the polymer can cause compaction of the structure of the nanocomposite membrane.[86]

Table 1 WU and MS measured for the membrane by RSM as a function of temperature

Run	DS (%)	S-TaS_2 (%)	WU@20 °C (%)	WU@40 °C (%)	WU@60 °C (%)	WU@80 °C (%)	MS@20 °C (%)	MS@40 °C (%)	MS@60 °C (%)	MS@80 °C (%)
1	67.50	1.50	40.87	44.78	49.4	61.81	8.53	10.09	12.07	14.65
2	67.50	1.50	40.51	44.45	49.11	62.48	8.02	9.43	11.41	13.78
3	71.25	1.00	39.17	43.25	48.02	60.23	10.88	13.14	15.12	18.65
4	67.50	2.50	40.02	44.11	48.71	61.01	7.12	8.26	10.24	12.25
5	67.50	1.50	41.12	45.11	49.61	62.04	9.02	10.71	12.68	15.45
6	67.50	1.50	40.33	44.32	48.97	61.31	8.71	10.31	12.29	14.94
7	67.50	0.50	34.46	39.01	44.21	55.84	10.18	12.23	14.21	17.46
8	75.00	1.50	47.35	50.61	54.65	75.36	13.46	16.51	18.48	23.03
9	63.75	1.00	33.54	38.19	43.47	54.98	6.14	6.98	8.96	10.59
10	60.00	1.50	32.47	37.22	42.62	53.99	5.18	5.73	7.71	8.96
11	71.25	2.00	46.68	50.01	54.11	71.32	8.84	10.49	12.47	15.18
12	63.75	2.00	38.94	43.05	47.84	60.01	5.56	6.23	8.21	9.62
13	67.50	1.50	40.03	44.03	48.72	61.03	9.01	10.71	12.68	15.45

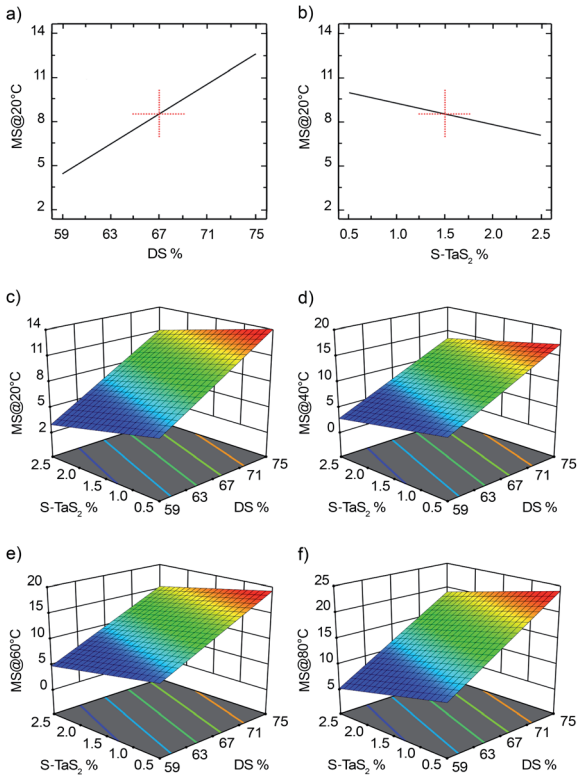

Fig. 4 One-factor effect plots illustrating the effect of: (a) DS of SPEEK on the MS at 1.5 wt% of S-TaS_2 nanoflakes, (b) wt% of S-TaS_2 nanoflakes on the MS at a DS of SPEEK of 67.50%. 3D-surface plots of MS *versus* DS of SPEEK and wt% of S-TaS_2 nanoflakes in the membranes, at the temperatures of (c) 20, (d) 40, (e) 60, and (f) 80 °C.

As shown in Table 1, for all the nanocomposite membranes investigated by the RSM, the MS increases upon increasing the temperature, similarly to the WU results.

It is important to note that the strong hydrogen bonding between functionalized groups of S-TaS_2 nanoflakes and sulfonated groups of polymer prevents excessive swelling of the nanocomposite membranes at high temperatures and increases the mechanical stability of nanocomposite membranes in DMFC conditions.[87]

2.2.2 Membrane proton conductivity. Proton transfer is the most important parameter for PEMs since it directly determines the final performance of DMFCs.[88] In particular, σ values are closely related to WU, temperature, and additive content.[89] The water molecules have a direct impact on σ of PEMs owing to their ability to form a hydrogen bonding network with sulfonated groups of nanoflakes and SPEEK and the role of these hydrogen bonding in both proton transfer mechanisms, *e.g.*, vehicle mechanism and Grotthuss (hopping) mechanism.[81,90] In the vehicle mechanism, the protons are carried by the free water molecules that form H_3O^+ complexes which then migrates through transfer channels of the PEM.[32] In the Grotthuss mechanism (proton hopping), protons jumped from one bound water molecule ($H_3O^+SO_3^-$) to the next through the formation and breaking of hydrogen bonding.[81] Protons supplied by $-SO_3H$ groups attached to the polymer backbone can attach to free water molecules through multiple hydrogen bonding to organize the hydrophilic regions and create well-aligned transfer channels.[91] Generally, both mechanisms are not independent in the PEMs and could make cooperative contributions to proton transfer. To verify the positive effect of S-TaS_2 nanoflakes in increasing the number of proton hopping sites to improve the σ of the as-prepared PEM, impedance spectroscopy was performed at different temperatures. The measured σ of the investigated nanocomposite membranes as a function of temperature, ranging from 20 to 80 °C, are shown in Table 2 and Fig. 5.

Clearly, the sulfonated groups in the nanocomposite membranes facilitate the ion transfer by acting as proton carriers. In particular, by increasing the DS of SPEEK, σ improves because the hydrophilicity of the polymer increases with the number of hydrophilic sulfonated groups. Fig. 5a shows that the highest DS of polymer (75%) results in a maximum σ (110 mS cm^{-1}). Nevertheless, the optimum percentage of DS for the polymer also needs to consider the *P* of the membrane, as well as the mechanical properties of the resulting membrane electrode assemblies (MEA). The RSM analysis has shown that the σ of the nanocomposite membranes increases with increasing wt% of S-TaS_2 nanoflakes. The maximum σ is reached for wt% of S-TaS_2 nanoflakes

Table 2 σ, *P* and *S* measured for the investigated membranes by RSM (M_{runx}) as a function of temperature

Run	DS (%)	S-TaS_2 (%)	σ@20 °C (mS cm^{-1})	σ@40 °C (mS cm^{-1})	σ@60 °C (mS cm^{-1})	σ@80 °C (mS cm^{-1})	*P* $\times 10^{-7}$ (cm^2 S^{-1})	$S \times 10^4$ (S s cm^{-3})
1	67.50	1.50	83.98	93.92	112.47	145.19	2.61	32.17
2	67.50	1.50	81.34	92.17	110.37	141.38	2.48	32.79
3	71.25	1.00	78.57	88.71	106.49	136.66	3.50	22.44
4	67.50	2.50	77.13	86.87	104.44	134.17	3.01	25.62
5	67.50	1.50	84.11	95.64	114.26	146.09	2.52	33.37
6	67.50	1.50	79.49	89.86	107.79	138.24	2.46	32.31
7	67.50	0.50	65.63	72.54	88.38	114.67	3.25	20.19
8	75.00	1.50	116.45	136.06	159.53	201.07	4.04	29.11
9	63.75	1.00	64.71	71.38	87.09	113.10	3.65	17.72
10	60.00	1.50	61.01	66.76	81.91	106.82	2.09	29.19
11	71.25	2.00	95.20	109.50	129.78	164.94	3.06	31.11
12	63.75	2.00	81.34	92.17	110.37	141.38	2.92	27.85
13	67.50	1.50	83.02	94.75	113.09	144.87	2.51	33.07

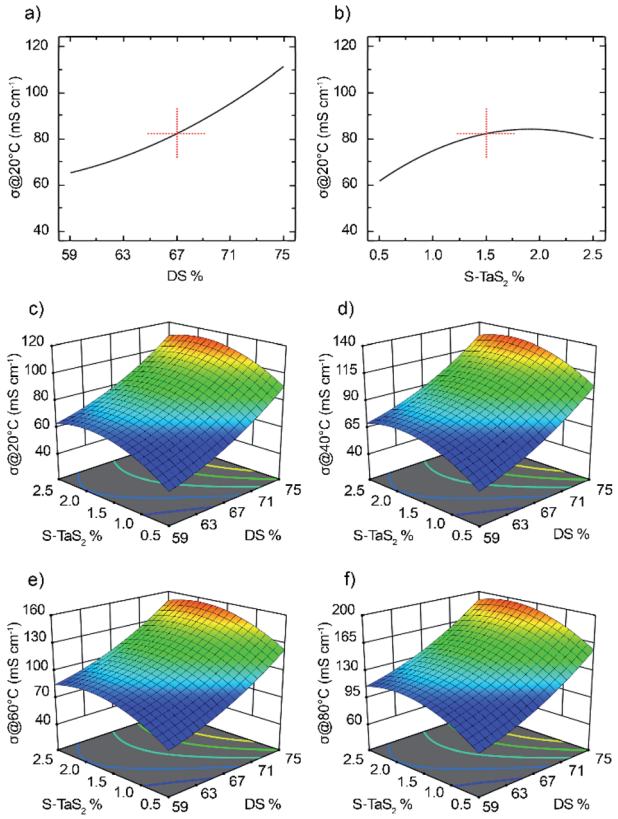

Fig. 5 One-factor effect plots illustrating the influence of (a) DS of SPEEK on σ at 1.5 wt% of S-TaS_2 nanoflakes and (b) wt% of S-TaS_2 nanoflakes on σ at a DS of 67.50%. 3D-surface plots of σ *versus* DS of SPEEK and wt% of S-TaS_2 nanoflakes in the membranes, at the temperatures of (c) 20, (d) 40, (e) 60, and (f) 80 °C.

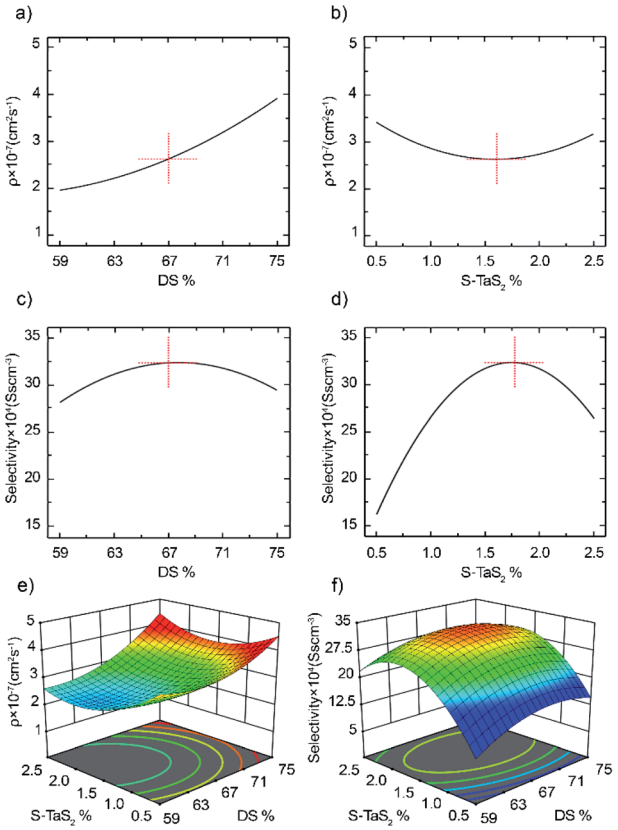

Fig. 6 One-factor effect plot illustrating the influence of: (a) DS of SPEEK on the *P* at 1.5 wt% of S-TaS_2 nanoflakes; (b) wt% of S-TaS_2 nanoflakes on the *P* at the DS of 67.50%, (c) DS of SPEEK on the *S* at 1.5 wt% of S-TaS_2 nanoflakes; and (d) wt% of S-TaS_2 nanoflakes on the *S* at the DS of SPEEK of 67.50%. 3D-surface plots of (e) *P* and (f) *S versus* DS of SPEEK and wt% of S-TaS_2 nanoflakes in the membranes at room temperature.

equal to 1.9, as a consequence of the increase of the bound water –SO_3H group contents in the PEMs *via* the Grotthuss mechanism.[31] According to their 2D structure, the S-TaS_2 nanoflakes have a high surface area functionalized with the sodium 3-mercapto-1-propane sulfonate salt (SMPS) molecules exhibiting –SO_3H groups. Therefore, S-TaS_2 nanoflakes can hold an elevated number of free water molecules, facilitating the transport of proton in the nanocomposite membrane. However, for S-TaS_2 exceeding 2 wt% in the composite, σ is reduced because of the aggregation of nanoflakes, which block the transfer channels responsible for the proton transfer through the polymeric matrix.[92] The results reported in Table 2 show that the σ of the membranes improves with the increase of the temperature, as a consequence of enhancement of the mobility of polymer chains and WU.[93]

2.2.3 Membrane methanol permeability and selectivity. Methanol permeation is one of the most important parameters determining the practical usability of the investigated membranes for DMFC applications. During the DMFC operation, the permeated methanol through the membranes could not only lead to a poor DMFC performance but also result in the poisoning of the cathode catalysts,[2] thus reducing the electrocatalytic activity. The results of Fig. 6 and Table 2 show that all the nanocomposite membranes exhibit excellent methanol blocking ability, which are reasonably attributed to the 2D structure of S-TaS_2 nanoflakes.[94–96] Fig. 6a and b shows the relation between the DS of the polymer and the weight percentage of S-TaS_2 nanoflakes and their impacts on *P* of the as-prepared membranes. By increasing the DS of polymer at a constant amount of nanoflakes (1.5 wt%), the methanol crossover increased (Fig. 6a). This effect is likely ascribed to the highly hydrophilic nature of membranes based on a high-DS polymer, which can result in more permeability to fuel (methanol) passing with water molecules. This explanation agrees with the trend observed for the WU of the investigated membranes. Importantly, the low *P* of SPEEK is attributed to the limited hydrophilic/hydrophobic region separation (hydrophobic backbone with hydrophilic branches).[18] However, an excessive amount of –SO_3H hydrophilic groups can disrupt this hydrophobic/hydrophilic phase separation, increasing the *P* in high-DS membranes. Remarkably, the *P* of the nanocomposite membranes significantly decreased with the increase of wt% of S-TaS_2 nanoflakes (Fig. 6b). Therefore, the addition of S-TaS_2 nanoflakes leads to high-DS membranes with low *P* due to the strong hydrogen bonding between the –SO_3H groups of the S-TaS_2 nanoflakes and the polymeric branches. The compact

morphology of the nanocomposite membranes that resulted from hydrogen bonding can be effective in preventing methanol permeation.[97] However, for wt% of S-TaS_2 nanoflakes higher than 1.7 wt%, the increase of hydrophilicity of the membrane is caused by the aggregation of S-TaS_2 nanoflakes (see X-ray spectroscopy (EDX) analysis in the next section), which can deteriorate the P of the membranes.[98] The M_{run10} has shown the lowest P (2.09×10^{-7} cm^2 S^{-1}), although the σ of this membrane is significantly inferior to those exhibited by other investigated membranes (*e.g.*, 61.01 mS cm^{-1}, see Table 2).

In DMFCs, it is essential for PEMs to maintain a high σ while reducing P. Therefore, S is one of the most important parameters to evaluate the potential of using novel membranes in DMFCs. The impact of the DS of polymer and nanoflake content in terms of S has been determined by means of RSM, as shown in Fig. 6c and d. The S results demonstrated in Table 2 show that the prepared nanocomposite membranes have good potential for use as a PEM in DMFC. The distinctive aggregation–separation of hydrophilic–hydrophobic domains and the sulfonated groups of PEMs play a key role in the selection of protons and methanol.[99] As shown in Fig. 6c and d, maximum S values are achieved at the DS of 69% and the wt% of S-TaS_2 nanoflakes of 1.8.

2.2.4 Membrane optimization. The aim of this study is the optimization of PEMs based on SPEEK and S-TaS_2 nanoflakes displaying high σ and S while maintaining low MS and P values. Due to the production of water molecules during the operation of the DMFC, the S and MS of the membrane have a simultaneous role in the final performance of DMFCs. By implementing our experimental results for the M_{runx} in the RSM and prioritizing their importance ($S > \sigma > P >$ MS > WU), the optimal DS of SPEEK and wt% of S-TaS_2 nanoflakes were statistically calculated. Table 3 shows the optimum membrane parameters calculated by RSM, *i.e.*, a wt% of S-TaS_2 nanoflakes of 1.9 and a DS of SPEEK of 70.2%. Noteworthily, RSM represents an effective group of statistical methods solving multivariate equations to predict the effect of multiple independent (*e.g.*, DS and wt% of S-TaS_2) and dependent variables (*e.g.*, WU, MS, P, S and σ) on the performance.[46,47] Table 4 shows the comparison between the experimental and RSM-simulated properties of SPEEK membrane (M_S) and optimized membrane (*i.e.*, M_{opt}), as determined by RSM. The experimental results agree well with the RSM-predicted data. Besides, the relative errors (E) between experimental and simulated results indicate that the process optimization by means of RSM is a reliable approach to optimize the novel type of membrane. Noteworthily, the performances measured for M_{opt} outperform those of M_{run5}, which resulted to be the best membrane among the M_{runx}. As shown in Fig. S1–S3,† M_S, M_{run5} and M_{opt} were further characterized in terms of structural properties, ion-exchange capacity and minimum energy required for transferring a proton (*i.e.*, activation energy, E_a) by performing Fourier-transform infrared spectroscopy measurements, conventional acid–base titration and Arrhenius plot analysis, respectively.

2.2.5 Membrane morphology. Fig. 7 shows the cross-sectional scanning electron microscopy (SEM) images of M_S and M_{opt} membranes. Both pristine and nanocomposite membranes show a dense and uniform morphology, without exhibiting any crack. Compared to the M_S membrane (Fig. 7a), the nanocomposite membrane (Fig. 7b) shows a rougher structure due to the presence of S-TaS_2 nanoflakes. Similar effects were observed in other SPEEK-based membranes using 2D additives.[100,101] Fig. 7c and d shows the EDX images of M_{opt} and M_{run4} (membrane with 2.5 wt% S-TaS_2 nanoflakes). As shown by the EDX map of Ta (Fig. 7c), the S-TaS_2 nanoflakes are homogeneously dispersed in the structure of M_{opt}, thanks to the strong interfacial hydrogen bonding between the sulfonated groups of S-TaS_2 nanoflakes and the SPEEK matrix.[101] However, the dispersion of S-TaS_2 nanoflakes in M_{run4} with 2.5 wt% of S-TaS_2 nanoflakes is inhomogeneous, evidencing nanoflakes agglomerates in some parts of the membrane (Fig. 7d). As shown in the previous sections, an excessive amount of S-TaS_2 nanoflakes compared to that of M_{opt} can fill the vacant sites available for the passage of free water molecules in the membrane, subsequently, reducing both WU and σ.

Table 3 Properties of the optimized membrane (M_{opt}) predicted by RSM

DS (%)	S-TaS_2 (%)	WU@ 20 °C (%)	WU@ 40 °C (%)	WU@ 60 °C (%)	WU@ 80 °C (%)	MS@ 20 °C (%)	MS@ 40 °C (%)	MS@ 60 °C (%)	MS@ 80 °C (%)	σ@20 °C (mS cm^{-1})	σ@40 °C (mS cm^{-1})	σ@60 °C (mS cm^{-1})	σ@80 °C (mS cm^{-1})	$P \times 10^{-7}$ (cm^2 s)	$S \times 10^4$ (S s cm^{-3})
70.2	1.9	44.77	48.30	52.56	68.13	9.41	11.24	13.22	16.15	92.65	107.41	126.21	160.61	2.77	33.44

Table 4 Measured properties of the optimized membrane (M_{opt}) at room temperature, validating the RSM-based membrane optimization approach

	WU (%)			MS (%)			σ (mS cm^{-1})			$P \times 10^{-7}$ (cm^2 s)			$S \times 10^4$ (S s cm^{-3})		
Membrane	Pre.	Exp.	E (%)	Pre.	Exp.	E (%)	Pre.	Exp.	E (%)	Pre.	Exp.	E (%)	Pre.	Exp.	E (%)
M_{opt}	44.77	45.72	2.05	9.41	9.64	2.38	92.65	96.24	3.73	2.77	2.66	3.97	33.44	36.18	7.57
M_{run5}		41.12			9.02			84.11			2.52			33.37	
M_S		37.46			15.31			43.32			6.86			6.31	

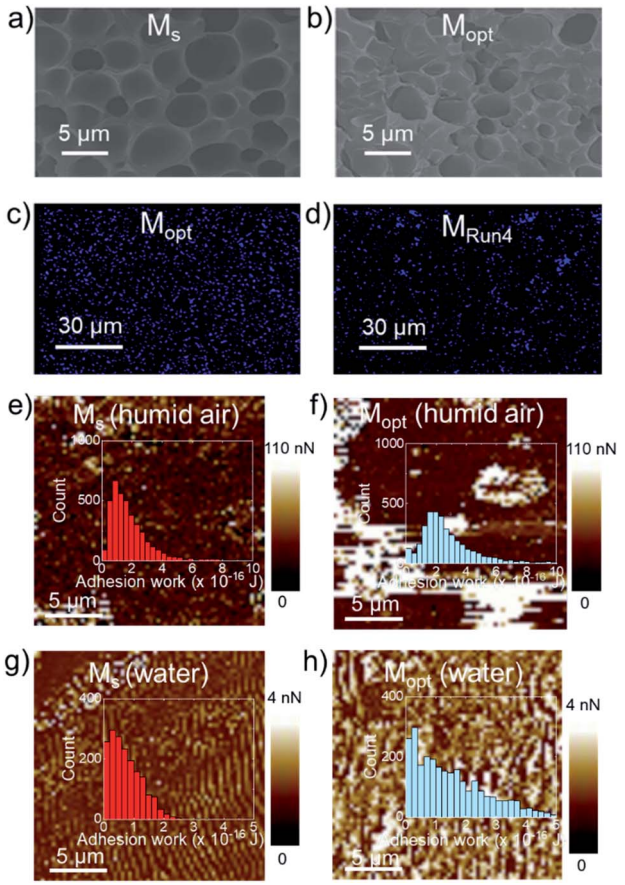

Fig. 7 Cross-sectional SEM images of (a) M_S and (b) M_{opt}. EDX maps of (c) M_{opt} and (d) M_{run4} for Ta (M line at 1.71 keV). (e–h) Adhesion force maps measured by AFM for M_S and M_{opt} in humid ambient air (panels e and f) and water (panels g and h). The adhesion work distributions of the corresponding adhesion force maps are also shown as insets to panels (e–h).

In addition, atomic force microscopy (AFM) measurements were carried out to identify the hydrophilic and hydrophobic domains of the investigated membranes. The adhesion properties of samples were first tested in humid ambient air (relative humidity RH ~ 75%). Subsequently, each sample was also evaluated in water (wet-state), thus "simulating" the working conditions of the membranes. By considering the Lennard-Jones force–separation relation,[102,103] the adhesion force measurements can identify the water accessible sites of the membranes, which are typically expressed by hydrophilic porous nano-/microdomains.[104–106]

In air, the adhesion force between the AFM tip and the membrane surface is dictated by the capillary force,[107] which depends on the hydrophilicity/hydrophobicity properties of the membrane.[104,105] In addition, in both air and water, the chemical specificity (*e.g.*, the presence of functional groups) of membranes strongly affects the pull-off force at the nano-/microscale level,[108,109] giving additional quantitative information regarding the presence of polar hydrophilic groups.

Fig. 7e–h shows the adhesion force maps measured for M_S and M_{opt} in humid air and water. In addition, the distributions of the work needed to detach the AFM tip from the sample (adhesion work), corresponding to the adhesion force maps, are also shown as insets to panels.

In humid ambient air, the mean adhesion works are 0.36 and 0.41 aJ for M_S and M_{opt}, respectively. In water, the difference between the adhesion works of the membranes is even more pronounced, the average values being 0.07 and 0.16 aJ for M_S and M_{opt}, respectively. Overall, these results indicate that M_{opt} exhibits more hydrophilic domains and polar functional groups compared to those of M_S. These features result in high WU, leading to high σ, in agreement with previous characterization data.

2.2.6 Mechanical, thermal, and oxidative stability. Besides their high S, effective PEMs must display adequate mechanical properties to be used in DMFCs.[33] Fig. S4† shows the stress–strain behavior of the M_S and M_{opt} membranes, allowing the tensile strength and elongation at break (E_b) of these membranes to be evaluated. The tensile strength of the M_{opt} membrane (36.4 MPa) is higher than that of the M_S membrane (32.5 MPa) because of the strong interaction between S-TaS_2 nanoflakes and the SPEEK matrix. Since the sulfonated groups of S-TaS_2 nanoflakes show a positive charge outward displacement, a compact structure is obtained by means of the electrostatic interaction between the nanoflakes and the polymer chains.[101] Thus, the homogeneous distribution of S-TaS_2 nanoflakes in the SPEEK matrix (see Fig. 7c) yields a superior mechanical stability of the M_{opt} nanocomposite membrane compared to that of M_S. Moreover, E_b decreases from 12.86% in the M_S membrane to 11.87% in the M_{opt} membrane. It is reasonable that the presence of S-TaS_2 nanoflakes decreases the mobility of the polymeric chains compared to that of the pristine polymer.

The thermal stability of the polymer is a key metric of PEM for DMFC operation at different temperatures. Therefore, thermogravimetric analysis (TGA) was carried out on the investigated PEMs to examine their thermal properties (Fig. S5†). Thanks to its rigid aromatic structure, SPEEK is considered a thermally stable polymer up to 300 °C. The TGA curves of M_S and M_{opt} membranes show a similar lineshape with three-step weight drop. The first mass loss occurred at the temperature of around 100 °C because of the expulsion of residual water and solvent. The second weight loss step observed for membranes, which occurred around 250 °C, is attributed to the decomposition of the sulfonated groups of SPEEK.[110] The M_{opt} nanocomposite membrane shows a lower weight loss compared to that of pristine SPEEK. This effect can be attributed to the hydrogen bonding between sulfonated groups of S-TaS_2 nanoflakes and the functionalized groups of SPEEK, which limit the membrane weight loss of the pristine polymer. The third weight loss, observed at 500 °C, marks the beginning of degradation and fragmentation of the main chain of SPEEK.[111] The lower weight loss of nanocomposite membranes indicates that the S-TaS_2 nanoflakes can also improve the thermal stability of the membrane due to the formation of hydrogen bonding with the polymer. According to the operation temperature of DMFCs (up to 80 °C), the

optimized nanocomposite membranes are expected to be an effective PEM for DMFCs.

Another important requirement for the long-term use of a PEM in DMFCs is the oxidative stability. The oxidative stabilities of M_S, M_{run5}, and M_{opt} membranes were investigated by immersing the prepared membranes in Fenton's reagent at 80 °C.

The oxidative stabilities of M_S, M_{run5}, and M_{opt} membranes were 2.3, 3.5, and 4.1 h, respectively. During DMFC operation, strong radical species such as hydroxyl (˙OH) and hydroperoxy (˙OOH) radicals are generated on electrodes from oxygen diffusion through the membrane and incomplete reduction at the DMFC cathode.[112] Such radicals can break the polymeric chains, leading to chemical degradation of the PEMs.[112] In particular, in Fenton's reagent, the Fe ions catalyze H_2O_2 to produce reactive ˙OOH radicals, which degrade the PEM structure.[88] The oxidative stability results have shown that the addition of S-TaS_2 nanoflakes to the SPEEK matrix plays an important role in suppressing the degradation of nanocomposite membranes from radical-induced degradation. Typically, the oxidative stability of the membrane has a reverse relation to the MS.[113] The nanocomposite membranes with lower MS provide a lower chance for harmful radicals to attack the polar groups of SPEEK.[22] Our results agree with these phenomenological expectations.

2.2.7 Nanocomposite membrane validation in DMFCs. To validate the practical potential of optimized nanocomposite membranes, the M_S, M_{run5}, and M_{opt} were selected for the fabrication and characterization of DMFCs. The M_{run5} shows the best results (σ and S) compared to other prepared nanocomposite membranes listed in Table 2. The polarization and performance curves of the membranes at temperatures of 30, 60, and 80 °C are summarized in Fig. 8. By comparing the performances of pristine SPEEK and nanocomposite membranes, the effect of the addition of S-TaS_2 nanoflakes to polymer chains on the DMFC performance was evaluated.

Fig. 8a shows the voltage–current curves of the investigated membranes at room temperature. Fig. 8a shows that the M_{opt} has a higher open-circuit voltage (OCV) than the other produced membranes. The high OCV of the M_{opt} suggests that the fuel (methanol) crossover across this nanocomposite membrane is lower than that across pristine SPEEK due to the lower P,[114] as shown in Table 4. In comparison with the M_S, the voltage–current curves of the cell with nanocomposite membranes show a remarkable enhancement of performance at room temperature. The cell assembled with M_{opt} exhibited the best performance, achieving a maximum power density of 64.55 mW cm^{-2} and a maximum current density of 265.3 mA cm^{-2}, which are about 78% higher than those of M_S (with a maximum power density of 36.12 mW cm^{-2} and a maximum current density of 194.1 mA cm^{-2}) and 8% higher than those of M_{run5} (with a maximum power density of 60.01 mW cm^{-2} and a maximum current density of 256.8 mA cm^{-2}).

These results are explained by the superior σ and limited methanol permeation (relative to the M_S, *i.e.*, pristine SPEEK) provided by the optimal wt% of S-TaS_2 nanoflakes in the nanocomposite membrane. Fig. 8b shows the polarization curves of the M_{opt} at different temperatures. The maximum

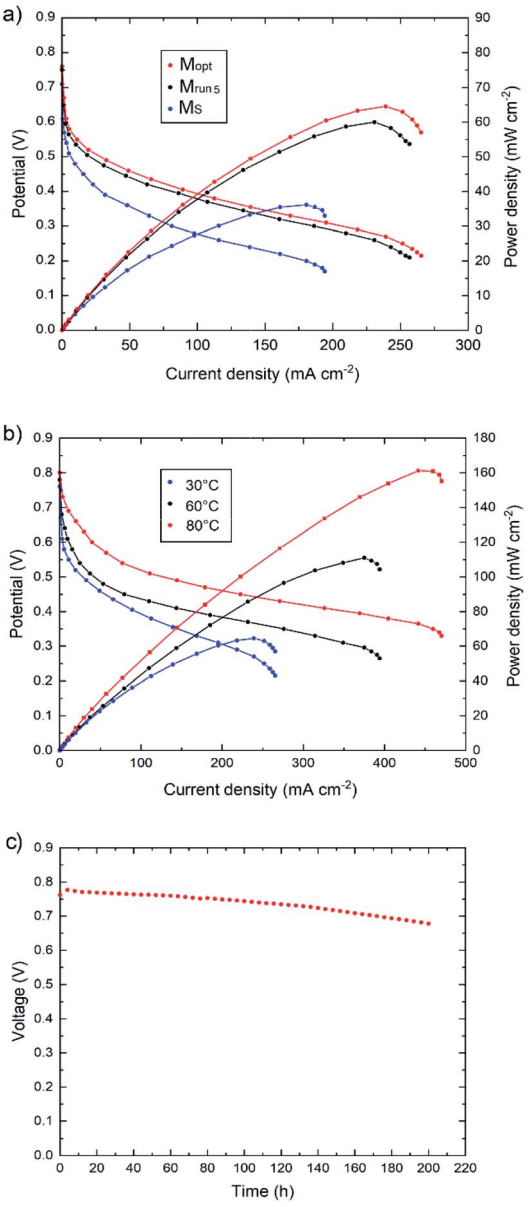

Fig. 8 Polarization curves of (a) M_S, M_{run5} and M_{opt} at 30 °C and (b) M_{opt} at different temperatures. (c) Time dependence of the OCV of the DMFC assembled with the M_{opt} at room temperature.

power densities of M_{opt} are 64.55, 111.02, and 161.18 mW cm^{-2} with maximum current densities of 265.3, 393.9, and 470.1 mA cm^{-2} at 30, 60, and 80 °C, respectively. These results match well with the dependency of σ on the temperature. As shown in Table 2, the σ increases with increasing temperature, consequently improving the final power density performance of the DMFCs.

The long-term stability of the M_{opt} during DMFC operation was evaluated by recording the OCV of the corresponding cell for 200 h, and the obtained results are shown in Fig. 8c. The OCV of the cell almost retained its initial value after 200 h, showing an OCV fading rate as low as 0.42 mV h^{-1}. The performance stability of the M_{opt} is attributed to its water retention ability along with high MS (9.64%) and mechanical stability (TS = 36.4 MPa).[34,115]

Table S7† reports a comparison between WU, σ, P, and power density of the M_{opt} with Nafion- and SPEEK-based membranes reported in the literature. Importantly, our nanocomposite membranes exhibit σ and power density that are significantly superior to those of Nafion- and SPEEK-based membranes reported in the literature.[12,116–122]

3. Conclusions

In summary, we have shown the fabrication and characterization of novel nanocomposite PEMs based on SPEEK and S-TaS_2, to overcome the high methanol permeability ($P > 10^{-7}$ cm^2 s^{-1}) and membrane swelling (>20%) of the SPEEK membrane with high DS.[87] Thanks to the metallic character of their natural stable phases, 2D 6R-TaS_2 nanoflakes are easily functionalized using sodium 3-mercapto-1-propane sulfonate salt. The sulfonated groups in S-TaS_2 positively affect their proton-conducting ability, further enhancing the σ of SPEEK. Besides, the presence of sulfonated groups in TaS_2 nanoflakes improves the dispersion of nanoflakes in the solvent used to process SPEEK, allowing the flakes to be homogeneously dispersed in the polymeric matrix. Meanwhile, the interfacial interactions and formation of strong hydrogen bonding between sulfonated groups of S-TaS_2 nanoflakes and functionalized groups of SPEEK promote the compactness of the PEM structure, increasing the dimensional, thermal, and chemical stability of the nanocomposite membrane. Using CCD in DOE software as the experimental design for our multivariable system, the membranes are optimized to reach an optimum power density. Our results prove that the nanocomposite membrane with a DS of 70.2% and wt% of S-TaS_2 nanoflakes of 1.9 is the optimum PEM (M_{opt}) for DMFCs. In particular, the P of the M_{opt} membranes decreased to 2.66×10^{-7} cm^2 s^{-1} compared to 6.86×10^{-7} cm^2 s^{-1} of the pristine SPEEK. Meanwhile, both σ and P increased compared to those of pristine SPEEK, reaching 96.24 mS cm^{-1} and 36.18×10^4 S s cm^{-3}, respectively. Our nanocomposite membranes show a maximum power density of 64.55 mW cm^{-2} with a maximum current density of 265.3 mA cm^{-2} at room temperature, which is ~78% higher than the maximum current density of the pristine SPEEK (maximum power density of 36.12 mW cm^{-2}). These results indicate that the chemical interaction between the S-TaS_2 nanoflakes and polymer can be advantageously exploited to improve the performance of SPEEK. Overall, our results support that TaS_2 nanoflakes can be functionalized by sulfonated groups to act as an efficient fuel barrier additive for PEMs with superior ionic conductivity compared to that of pristine polymer. Therefore, our nanocomposite membranes are promising PEMs for DMFCs.

Conflicts of interest

There are no conflicts to declare.

Acknowledgements

This project received funding from the European Union's Horizon 2020 Research and Innovation Program under grant agreement No. 785219-GrapheneCore3, the MSCA-ITN ULTIMATE project under grant agreement No. 813036, the Bilateral project GINSENG between NSFC (China) and MAECI (Italy) (2018–2020), and Natural Science Foundation of Shandong Province (ZR2019QEM009). We thank the Electron Microscopy and the Materials Characterization facilities – Istituto Italiano di Tecnologia for providing support regarding SEM/TEM and XPS data acquisition, respectively. The project was supported by Czech Science Foundation (GACR No. 20-16124J).

Notes and references

1 R. K. Mallick, S. B. Thombre and N. K. Shrivastava, *Renewable Sustainable Energy Rev.*, 2016, **56**, 51–74.
2 H. Beydaghi, M. Javanbakht, A. Bagheri, H. Ghafarian-Zahmatkesh and K. Hooshyari, *Iran. J. Hydrogen Fuel Cell*, 2017, **4**, 1–11.
3 Q. Tan, T. Qu, C. Shu, Y. Liu, Y. He, W. Zhai, S. Guo, L. Liu and Y. Liu, *ACS Sustainable Chem. Eng.*, 2019, **7**, 17145–17153.
4 W. Yuan, A. Wang, G. Ye, B. Pan, K. Tang and H. Chen, *Appl. Energy*, 2017, **188**, 431–443.
5 J. Zheng, L. Dai, S. Li, C. Shi, Y. Li, S. Zhang, H. Yang and T. A. Sherazi, *ACS Appl. Energy Mater.*, 2018, **1**, 941–947.
6 F. Bonaccorso, L. Colombo, G. Yu, M. Stoller, V. Tozzini, A. C. Ferrari, R. S. Ruoff and V. Pellegrini, *Science*, 2015, **347**, 1246501.
7 P. Salarizadeh, M. Javanbakht, S. Pourmahdian, A. Bagheri, H. Beydaghi and M. Enhessari, *J. Colloid Interface Sci.*, 2016, **472**, 135–144.
8 A. Bagheri, M. Javanbakht, P. Hosseinabadi, H. Beydaghi and A. Shabanikia, *Polymer*, 2018, **138**, 275–287.
9 V. Guccini, A. Carlson, S. Yu, G. Lindbergh, R. W. Lindström and G. Salazar-Alvarez, *J. Mater. Chem. A*, 2019, **7**, 25032–25039.
10 H. Beydaghi, A. Bagheri, P. Salarizadeh, S. Kashefi, K. Hooshyari, A. Amoozadeh, T. Shamsi, F. Bonaccorso and V. Pellegrini, *Ind. Eng. Chem. Res.*, 2020, **59**, 6589–6599.
11 C. Minke and T. Turek, *J. Power Sources*, 2015, **286**, 247–257.
12 Q. He, J. Zheng and S. Zhang, *J. Power Sources*, 2014, **260**, 317–325.
13 K. Hooshyari, S. N. Khanamiri, P. Salarizadeh and H. Beydaghi, *J. Electrochem. Soc.*, 2019, **166**, F976–F989.
14 K.-D. Kreuer, *Chem. Mater.*, 2014, **26**, 361–380.
15 J. Miyake, T. Mochizuki and K. Miyatake, *ACS Macro Lett.*, 2015, **4**, 750–754.
16 D. W. Shin, M. D. Guiver and Y. M. Lee, *Chem. Rev.*, 2017, **117**, 4759–4805.
17 T. Luo, Y. Zhang, H. Xu, Z. Zhang, F. Fu, S. Gao, A. Ouadah, Y. Dong, S. Wang and C. Zhu, *J. Membr. Sci.*, 2016, **514**, 527–536.
18 A. Bagheri, P. Salarizadeh, M. Sabooni Asre Hazer, P. Hosseinabadi, S. Kashefi and H. Beydaghi, *Electrochim. Acta*, 2019, **295**, 875–890.
19 K. Hooshyari, S. Heydari, M. Javanbakht, H. Beydaghi and M. Enhessari, *RSC Adv.*, 2020, **10**, 2709–2721.

20 R. S. L. Yee, R. A. Rozendal, K. Zhang and B. P. Ladewig, *Chem. Eng. Res. Des.*, 2012, **90**, 950–959.
21 A. Amoozadeh, H. Mazdarani, H. Beydaghi, E. Tabrizian and M. Javanbakht, *New J. Chem.*, 2018, **42**, 16855–16862.
22 Y. Liang, C. Gong, Z. Qi, H. Li, Z. Wu, Y. Zhang, S. Zhang and Y. Li, *J. Power Sources*, 2015, **284**, 86–94.
23 T. Maharana, A. K. Sutar, N. Nath, A. Routaray, Y. S. Negi and B. Mohanty, *Adv. Energy Mater.*, 2014, 433–464.
24 A. Iulianelli and A. Basile, *Int. J. Hydrogen Energy*, 2012, **37**, 15241–15255.
25 D. Brush, M. Danilczuk and S. Schlick, *Macromolecules*, 2015, **48**, 637–644.
26 J. S. Lawton and D. E. Budil, *J. Membr. Sci.*, 2010, **357**, 47–53.
27 H. Beydaghi, M. Javanbakht, P. Salarizadeh, A. Bagheri and A. Amoozadeh, *Polymer*, 2017, **119**, 253–262.
28 Y.-H. Su, Y.-L. Liu, Y.-M. Sun, J.-Y. Lai, M. D. Guiver and Y. Gao, *J. Power Sources*, 2006, **155**, 111–117.
29 S. Khilari, S. Pandit, M. M. Ghangrekar, D. Pradhan and D. Das, *Ind. Eng. Chem. Res.*, 2013, **52**, 11597–11606.
30 D. C. Lee, H. N. Yang, S. H. Park and W. J. Kim, *J. Membr. Sci.*, 2014, **452**, 20–28.
31 H. Beydaghi, M. Javanbakht and E. Kowsari, *Ind. Eng. Chem. Res.*, 2014, **53**, 16621–16632.
32 H. Beydaghi and M. Javanbakht, *Ind. Eng. Chem. Res.*, 2015, **54**, 7028–7037.
33 H. Beydaghi, M. Javanbakht, A. Bagheri, P. Salarizadeh, H. G. Zahmatkesh, S. Kashefi and E. Kowsari, *RSC Adv.*, 2015, **5**, 74054–74064.
34 H. Beydaghi, M. Javanbakht and E. Kowsari, *Polymer*, 2016, **87**, 26–37.
35 C. Ataca and S. Ciraci, *J. Phys. Chem. C*, 2011, **115**, 13303–13311.
36 S. S. Chou, M. De, J. Kim, S. Byun, C. Dykstra, J. Yu, J. Huang and V. P. Dravid, *J. Am. Chem. Soc.*, 2013, **135**, 4584–4587.
37 D. Voiry, A. Goswami, R. Kappera, C. de C. C. e. Silva, D. Kaplan, T. Fujita, M. Chen, T. Asefa and M. Chhowalla, *Nat. Chem.*, 2015, **7**, 45–49.
38 L. Najafi, S. Bellani, R. Oropesa-Nuñez, B. Martín-García, M. Prato, L. Pasquale, J.-K. Panda, P. Marvan, Z. Sofer and F. Bonaccorso, *ACS Catal.*, 2020, **10**, 3313–3325.
39 I. Raj, Y. Duan, D. Kigen, W. Yang, L. Hou, F. Yang and Y. Li, *Front. Mater. Sci.*, 2018, **12**, 239–246.
40 Y. Feng, S. Gong, E. Du, X. Chen, R. Qi, K. Yu and Z. Zhu, *J. Phys. Chem. C*, 2018, **122**, 2382–2390.
41 L. Najafi, S. Bellani, R. Oropesa-Nuñez, R. Brescia, M. Prato, L. Pasquale, C. Demirci, F. Drago, B. Martín-García, J. Luxa, L. Manna, Z. Sofer and F. Bonaccorso, *Small*, 2020, **16**, 2003372.
42 Y. Cui, S. I. Kundalwal and S. Kumar, *Carbon*, 2016, **98**, 313–333.
43 Y. Su, V. G. Kravets, S. L. Wong, J. Waters, A. K. Geim and R. R. Nair, *Nat. Commun.*, 2014, **5**, 4843.
44 S. Ayyaru and S. Dharmalingam, *Energy*, 2015, **88**, 202–208.
45 F. Dong, Z. Li, S. Wang, L. Xu and X. Yu, *Int. J. Hydrogen Energy*, 2011, **36**, 3681–3687.
46 A. Rahnavard, S. Rowshanzamir, M. J. Parnian and G. R. Amirkhanlou, *Energy*, 2015, **82**, 746–757.
47 H. Ilbeygi, A. Mayahi, A. F. Ismail, M. M. Nasef, J. Jaafar, M. Ghasemi, T. Matsuura and S. M. J. Zaidi, *J. Taiwan Inst. Chem. Eng.*, 2014, **45**, 2265–2279.
48 https://www.itl.nist.gov/div898/handbook/pri/section3/pri3361.htm.
49 https://www.statease.com/software/design-expert/.
50 E. Figueroa, Y.-K. Kuo, A. Olinger, M. A. Lloyd, L. D. Bastin, S. Petrotsatos, Q. Chen, B. Dobbs, S. Dev, J. P. Selegue, L. E. DeLong, C. P. Brock and J. W. Brill, *J. Solid State Chem.*, 1995, **114**, 486–490.
51 S. F. Meyer, R. E. Howard, G. R. Stewart, J. V Acrivos and T. H. Geballe, *J. Chem. Phys.*, 1975, **62**, 4411–4419.
52 A. R. Beal, *J. Phys. C: Solid State Phys.*, 1978, **11**, 4583–4590.
53 L. Najafi, S. Bellani, B. Martín-García, R. Oropesa-Nuñez, A. E. Del Rio Castillo, M. Prato, I. Moreels and F. Bonaccorso, *Chem. Mater.*, 2017, **29**, 5782–5786.
54 S. Sugai, K. Murase, S. Uchida and S. Tanaka, *Solid State Commun.*, 1981, **40**, 399–401.
55 M. Hangyo, S.-I. Nakashima and A. Mitsuishi, *Ferroelectrics*, 1983, **52**, 151–159.
56 T. Hirata and F. S. Ohuchi, *Solid State Commun.*, 2001, **117**, 361–364.
57 J. R. Duffey, R. D. Kirby and R. V. Coleman, *Solid State Commun.*, 1976, **20**, 617–621.
58 W. Wen, Y. Zhu, C. Dang, W. Chen and L. Xie, *Nano Lett.*, 2019, **19**, 1805–1813.
59 O. R. Albertini, R. Zhao, R. L. McCann, S. Feng, M. Terrones, J. K. Freericks, J. A. Robinson and A. Y. Liu, *Phys. Rev. B*, 2016, **93**, 214109.
60 A. Molina-Sánchez and L. Wirtz, *Phys. Rev. B: Condens. Matter Mater. Phys.*, 2011, **84**, 155413.
61 J. Luxa, V. Mazánek, M. Pumera, P. Lazar, D. Sedmidubský, M. Callisti, T. Polcar and Z. Sofer, *Chem.–Eur. J.*, 2017, **23**, 8082–8091.
62 E. Navarro-Moratalla, J. O. Island, S. Mañas-Valero, E. Pinilla-Cienfuegos, A. Castellanos-Gomez, J. Quereda, G. Rubio-Bollinger, L. Chirolli, J. A. Silva-Guillén, N. Agraït, G. A. Steele, F. Guinea, H. S. J. van der Zant and E. Coronado, *Nat. Commun.*, 2016, **7**, 11043.
63 L. Najafi, S. Bellani, R. Oropesa-Nuñez, B. Martín-García, M. Prato, V. Mazánek, D. Debellis, S. Lauciello, R. Brescia, Z. Sofer and F. Bonaccorso, *J. Mater. Chem. A*, 2019, **7**, 25593–25608.
64 C. J. Naumkin, A. V. Kraut-Vass, A. S. Gaarenstroomand W. Powell, *NIST Standard Reference Database 20, version 4.1 (web version)*, 2012.
65 T. Shimada, F. S. Ohuchi and A. Koma, *Surf. Sci.*, 1993, **291**, 57–66.
66 R. Hovden, A. W. Tsen, P. Liu, B. H. Savitzky, I. El Baggari, Y. Liu, W. Lu, Y. Sun, P. Kim, A. N. Pasupathy and L. F. Kourkoutis, *Proc. Natl. Acad. Sci. U. S. A.*, 2016, **113**, 11420–11424.
67 J. A. Wilson, F. J. Di Salvo and S. Mahajan, *Phys. Rev. Lett.*, 1974, **32**, 882–885.
68 J. Shi, X. Wang, S. Zhang, L. Xiao, Y. Huan, Y. Gong, Z. Zhang, Y. Li, X. Zhou, M. Hong, Q. Fang, Q. Zhang,

X. Liu, L. Gu, Z. Liu and Y. Zhang, *Nat. Commun.*, 2017, **8**, 958.
69 Z. Wang, Y.-Y. Sun, I. Abdelwahab, L. Cao, W. Yu, H. Ju, J. Zhu, W. Fu, L. Chu, H. Xu and K. P. Loh, *ACS Nano*, 2018, **12**, 12619–12628.
70 R. V Gonçalves, R. Wojcieszak, P. M. Uberman, S. R. Teixeira and L. M. Rossi, *Phys. Chem. Chem. Phys.*, 2014, **16**, 5755–5762.
71 S. Hellmann, M. Beye, C. Sohrt, T. Rohwer, F. Sorgenfrei, H. Redlin, M. Kalläne, M. Marczynski-Bühlow, F. Hennies, M. Bauer, A. Föhlisch, L. Kipp, W. Wurth and K. Rossnagel, *Phys. Rev. Lett.*, 2010, **105**, 187401.
72 M. Z. Xie, J. Y. Zhou, H. Ji, Y. Ye, X. Wang, K. Jiang, L. Y. Shang, Z. G. Hu and J. H. Chu, *Appl. Phys. Lett.*, 2019, **115**, 121901.
73 M. I. Serna, S. H. Yoo, S. Moreno, Y. Xi, J. P. Oviedo, H. Choi, H. N. Alshareef, M. J. Kim, M. Minary-Jolandan and M. A. Quevedo-Lopez, *ACS Nano*, 2016, **10**, 6054–6061.
74 M. Donarelli, F. Bisti, F. Perrozzi and L. Ottaviano, *Chem. Phys. Lett.*, 2013, **588**, 198–202.
75 X. Chen, N. C. Berner, C. Backes, G. S. Duesberg and A. R. McDonald, *Angew. Chem., Int. Ed.*, 2016, **55**, 5803–5808.
76 M. Fantauzzi, B. Elsener, D. Atzei, A. Rigoldi and A. Rossi, *RSC Adv.*, 2015, **5**, 75953–75963.
77 D. Lichtman, J. H. Craig, V. Sailer and M. Drinkwine, *Appl. Surf. Sci.*, 1981, **7**, 325–331.
78 D. Brion, *Appl. Surf. Sci.*, 1980, **5**, 133–152.
79 L. Wang, N. Deng, G. Wang, J. Ju, B. Cheng and W. Kang, *ACS Appl. Mater. Interfaces*, 2019, **11**, 39979–39990.
80 M. Mandal, G. Huang and P. A. Kohl, *ACS Appl. Energy Mater.*, 2019, **2**, 2447–2457.
81 H. Beydaghi, M. Javanbakht and A. Badiei, *J. Nanostruct. Chem.*, 2014, **4**, 97.
82 Z. Long, Y. Zhang, J. Miyake and K. Miyatake, *Ind. Eng. Chem. Res.*, 2019, **58**, 9915–9920.
83 X. Liang, G. Pan, L. Xu and J. Wang, *Fuel*, 2015, **139**, 393–400.
84 A. Mayahi, A. F. Ismail, H. Ilbeygi, M. H. D. Othman, M. Ghasemi, M. N. A. M. Norddin and T. Matsuura, *Sep. Purif. Technol.*, 2013, **106**, 72–81.
85 C. Ru, Y. Gu, H. Na, H. Li and C. Zhao, *ACS Appl. Mater. Interfaces*, 2019, **11**, 31899–31908.
86 M. Ionita, M. A. Pandele and H. Iovu, *Carbohydr. Polym.*, 2013, **94**, 339–344.
87 A. Bagheri, M. Javanbakht, H. Beydaghi, P. Salarizadeh, A. Shabanikia and H. Salar Amoli, *RSC Adv.*, 2016, **6**, 39500–39510.
88 L. Fu, G. Xiao and D. Yan, *ACS Appl. Mater. Interfaces*, 2010, **2**, 1601–1607.
89 T. Yang, Z. Li, H. Lyu, J. Zheng, J. Liu, F. Liu, Z. Zhang and H. Rao, *RSC Adv.*, 2018, **8**, 15740–15753.
90 X.-M. Li, J. Liu, C. Zhao, J.-L. Zhou, L. Zhao, S.-L. Li and Y.-Q. Lan, *J. Mater. Chem. A*, 2019, **7**, 25165–25171.
91 M. Wang, H.-B. Luo, J. Zhang, S.-X. Liu, C. Xue, Y. Zou and X.-M. Ren, *Dalton Trans.*, 2017, **46**, 7904–7910.
92 Y. Heo, H. Im and J. Kim, *J. Membr. Sci.*, 2013, **425–426**, 11–22.
93 C.-Y. Tseng, Y.-S. Ye, K.-Y. Kao, J. Joseph, W.-C. Shen, J. Rick and B.-J. Hwang, *Int. J. Hydrogen Energy*, 2011, **36**, 11936–11945.
94 T. Bayer, B. V Cunning, R. Selyanchyn, M. Nishihara, S. Fujikawa, K. Sasaki and S. M. Lyth, *Chem. Mater.*, 2016, **28**, 4805–4814.
95 W. Dai, Y. Shen, Z. Li, L. Yu, J. Xi and X. Qiu, *J. Mater. Chem. A*, 2014, **2**, 12423–12432.
96 H.-C. Chien, L.-D. Tsai, C.-P. Huang, C. Kang, J.-N. Lin and F.-C. Chang, *Int. J. Hydrogen Energy*, 2013, **38**, 13792–13801.
97 H. Sun, B. Tang and P. Wu, *ACS Appl. Mater. Interfaces*, 2017, **9**, 35075–35085.
98 M. Wang, G. Liu, X. Cui, Y. Feng, H. Zhang, G. Wang, S. Zhong and Y. Luo, *Solid State Ionics*, 2018, **315**, 71–76.
99 J. Li, F. Bu, C. Ru, H. Jiang, Y. Duan, Y. Sun, X. Pu, L. Shang, X. Li and C. Zhao, *J. Mater. Chem. A*, 2020, **8**, 196–206.
100 Z. Jiang, X. Zhao and A. Manthiram, *Int. J. Hydrogen Energy*, 2013, **38**, 5875–5884.
101 Y. Zhang, H. Wang, B. Liu, J. Shi, J. Zhang and H. Shi, *J. Mater. Chem. A*, 2019, **7**, 12669–12680.
102 J. E. Lennard-Jones, *Proc. Phys. Soc.*, 1931, **43**, 461–482.
103 N. Yu and A. A. Polycarpou, *J. Colloid Interface Sci.*, 2004, **278**, 428–435.
104 M. Farshchi-Tabrizia, M. Kappl and H.-J. Butt, *J. Adhes. Sci. Technol.*, 2008, **22**, 181–203.
105 L. Najafi, R. Oropesa-Nuñez, B. Martín-García, F. Drago, M. Prato, V. Pellegrini, F. Bonaccorso and S. Bellani, *Mater. Adv.*, 2020, **1**, 387–402.
106 L. Vannozzi, L. Ricotti, T. Santaniello, T. Terencio, R. Oropesa-Nunez, C. Canale, F. Borghi, A. Menciassi, C. Lenardi and I. Gerges, *J. Mech. Behav. Biomed. Mater.*, 2017, **75**, 147–159.
107 D. L. Sedin and K. L. Rowlen, *Anal. Chem.*, 2000, **72**, 2183–2189.
108 E. W. van der Vegte and G. Hadziioannou, *Langmuir*, 1997, **13**, 4357–4368.
109 C. D. Frisbie, L. F. Rozsnyai, A. Noy, M. S. Wrighton and C. M. Lieber, *Science*, 1994, **265**, 2071–2074.
110 T. Y. Inan, H. Doğan, E. E. Unveren and E. Eker, *Int. J. Hydrogen Energy*, 2010, **35**, 12038–12053.
111 N. Wang, S. Peng, Y. Li, H. Wang, S. Liu and Y. Liu, *J. Solid State Electrochem.*, 2012, **16**, 2169–2177.
112 G. Rambabu and S. D. Bhat, *Electrochim. Acta*, 2015, **176**, 657–669.
113 F. Bu, Y. Zhang, L. Hong, W. Zhao, D. Li, J. Li, H. Na and C. Zhao, *J. Membr. Sci.*, 2018, **545**, 167–175.
114 Y. Zhang, J. Miyake, R. Akiyama, R. Shimizu and K. Miyatake, *ACS Appl. Energy Mater.*, 2018, **1**, 1008–1015.
115 W. Zhengbang, H. Tang and P. Mu, *J. Membr. Sci.*, 2011, **369**, 250–257.
116 M. Gang, G. He, Z. Li, K. Cao, Z. Li, Y. Yin, H. Wu and Z. Jiang, *J. Membr. Sci.*, 2016, **507**, 1–11.
117 X. Liu, Y. Zhang, S. Deng, C. Li, J. Dong, J. Wang, Z. Yang, D. Wang and H. Cheng, *ACS Appl. Energy Mater.*, 2018, **1**, 5463–5473.

118 Z.-J. Jiang, Z. Jiang, X. Tian, L. Luo and M. Liu, *ACS Appl. Mater. Interfaces*, 2017, **9**, 20046–20056.
119 X. Liu, Y. Zhang, S. Deng, C. Li, J. Dong, J. Wang, Z. Yang, D. Wang and H. Cheng, *Chin. Chem. Lett.*, 2019, **30**, 299–304.
120 C. Dong, Q. Wang, C. Cong, X. Meng and Q. Zhou, *Int. J. Hydrogen Energy*, 2017, **42**, 10317–10328.
121 L. Lei, X. Zhu, J. Xu, H. Qian, Z. Zou and H. Yang, *J. Power Sources*, 2017, **350**, 41–48.
122 J.-C. Tsai and C.-K. Lin, *J. Taiwan Inst. Chem. Eng.*, 2011, **42**, 281–285.